Investigation of the Performance of a Syngas Quench Cooling Design in a Downdraft Entrained-Flow Gasifier

Ting Wang and Xijia Lu
twang@uno.edu, xlv@uno.edu
Energy Conversion& Conservation Center
University of New Orleans
New Orleans, LA 70148, USA

Heng-Wen Hsu and Cheng-Hsien Shen
hsuhw@itri.org.tw, CHShen@itri.org.tw
Green Energy and Environment Research Laboratory
Industrial Technology Research Institute
Taiwan 310, R.O.C.

ABSTRACT

Syngas coming out of a gasifier is usually very hot. Cooling is necessary to allow this syngas to be transported without damaging downstream piping or equipment. Furthermore, the existing cold syngas cleaning technology also requires that the syngas temperature to be reduced below 600^{o}F. Direct water quenching of syngas is one of the cooling schemes that can not only provide the necessary cooling, but also help to drive the water-gas shift (WGS) reaction to convert steam and carbon monoxide to carbon dioxide and hydrogen, which is an important process for systems implementing carbon capture and sequestration (CCS). To assist designing an adequate syngas quench cooling section, this study has employed computational fluid dynamics (CFD) to investigate the performance of a preliminary design of a water quench system in a downdraft entrained flow coal gasifier. The preliminary quench system design consists of a primary water curtain section located in the main entrance of the quench section and a secondary water spray section distributed in the outer annular passage with a counter-flow arrangement. The bottom water bath level can be adjusted to change the syngas's local speed over the water surface to fine-tune the WGS reaction without using more sprayed water. The main goal of this study is to use the experimental results to calibrate the CFD model, especially the WGS reaction model, and then to use the calibrated model to help design different water spray strategies to achieve the targeted temperature and syngas composition.

The result shows that three different reaction rates (Jones' rate under a catalytic condition, Wade's rate, and Sato's rate under a non-catalytic condition) are all too fast when comparing the CFD results against the experimental data. The exponential constant value (A) of each reaction rate is therefore adjusted to match the experiment data within 2 percentage points (or 6%) in both CO conversion rate and H_2 generation. The effect of the injection locations (primary vs. secondary) on WGS is marginal. Both locations result in 16% CO conversion rate. Spraying water in the primary location only provides a marginal advantage: an increase of 4% in H_2 production, 3% in HHV value, and 30K in temperature. Using water bath level to fine-tune the WGS reaction is workable. When the water level gap decreases from 1050mm to 700 mm, the CO conversion rate decreases 7 percentage points (or 35%) from 20% to 13%, and the syngas outlet temperature decreases by 20K (from 891 K to 871 K.) Beyond the gap of 1050mm, the effect of the water bath level is not noticeable.

INTRODUCTION

The Industrial Technology Research Institute (ITRI) has installed and operated a small, experimental, oxygen-blown, entrained-flow coal gasifier in Taiwan for six years (Wang et. al., 2006). In previous operations, dry, pulverized coal was pneumatically transported via nitrogen to the gasifier and injected from the bottom of the gasifier. This gasifier has been modified with a new design which requires that the feedstock be mixed with

water to form a coal slurry and be injected with oxygen from top of the gasifier, while the syngas exits near bottom of the gasifier (see Fig. 1a). The syngas is usually very hot (1400-1700K or 2200-2600^{o}F for oxygen-blown gasification) and needs to be cooled for two purposes: (a) so that it may be transported without damaging downstream piping materials or other equipment and (b) to satisfy the lower-temperature requirement of the desulfurization and other cleaning processes.

The syngas cooling process would significantly reduce the thermal efficiency of the system if care is not taken to employ the energy cascading scheme to properly maintain the grade (or quality) of the energy during the heat transfer process by applying cooling at different temperature ranges with an optimum pinch point for each cooling stage in a sequentially descending order. Radiant syngas coolers have been usually employed to achieve the highest thermal efficiency. However, a radiant syngas cooler is large, bulky, and expensive, so the direct syngas quenching process has also been adopted for the benefits of reduced space, cost, and maintenance, although it is accompanied by reduced thermal efficiency. A rule of thumb is that a gasification power generation system using a radiant syngas cooler will have approximately 2-3 percentage points higher thermal efficiency than a unit employing the quenching scheme. Recently, as carbon capture and sequestration (CCS) has become an important approach to curb global warming, the syngas quenching approach has become more popular in the gasification process because CCS typically employs the water-shift process (WGS) ($CO + H_2O \Leftrightarrow CO_2 + H_2$) to convert steam and CO to CO_2 and H_2, and, in this process, relatively low-temperature steam (below 600^{o}C, see Table 1) is required to allow the reaction to move in forward direction towards products. Since a large amount of relatively low-temperature steam is required, it might as well just directly employ quench cooling. This will allow preliminary water-shifting to occur and also utilize the quench chamber to serve as the first-stage shift reactor, thus reducing the cost of installing downstream WGS reactors. In addition to providing cooling and driving the WGS reaction, a water quench can also help clean out ash and other particulate matter. These additional benefits unfortunately are accompanied with another disadvantage: the unburned chars can also be washed away, causing a downgrade in the carbon conversion efficiency.

Table 1 Water-gas shift (WGS) reaction equilibrium balance constant

T(^{o}C)	600	800	1000	1200	1400
logK_p	1.396	0.553	0.076	-0.222	-0.424

Since there are many different means to design a quench chamber, conducting experiments to investigate many different options are a time consuming and expensive process. To help narrow down the number of experimental variables and to guide design development, the objective of this project is to employ Computational Fluid Dynamics (CFD) to investigate the syngas quench performance of a preliminary quench section design in a downdraft entrained-flow gasifier. The schematic of the preliminary design of the quench section is presented in Fig. 1b. The syngas flow enters the main chamber in the center of the quench section, impinges on the water bath surface, and deflects radially outward through eight openings to an annular outflow peripheral section that surrounds the main central chamber and is separated from the main chamber by a wall. The flow then moves upward and leaves the quench section through two outlets. The temperature and pressure of the incoming flow are 954 K and 3 atm, respectively. There are two injection locations: the primary one is located near the entrance of the quench section in the main flow chamber and another set of eight injectors serve as the secondary sprays. The primary injection provides the main water spray cooling with two pairs of opposing jets, separated 90^{o} apart. The secondary sprays are located in the annular duct and spray water downward against the up-flowing gas. This set of secondary injectors is used to aid in fine-tuning the temperature and syngas composition.

The water bath level can be adjusted higher or lower to allow the raw syngas to penetrate into the water bath at different depths to further reduce the syngas temperature, augment the WGS reaction, and remove soot and dust.

The main goal of this study is to use the experimental results to calibrate the CFD model, especially the WGS reaction model. Then, use the calibrated model to help design different water spray strategies to achieve the targeted temperature and syngas composition.

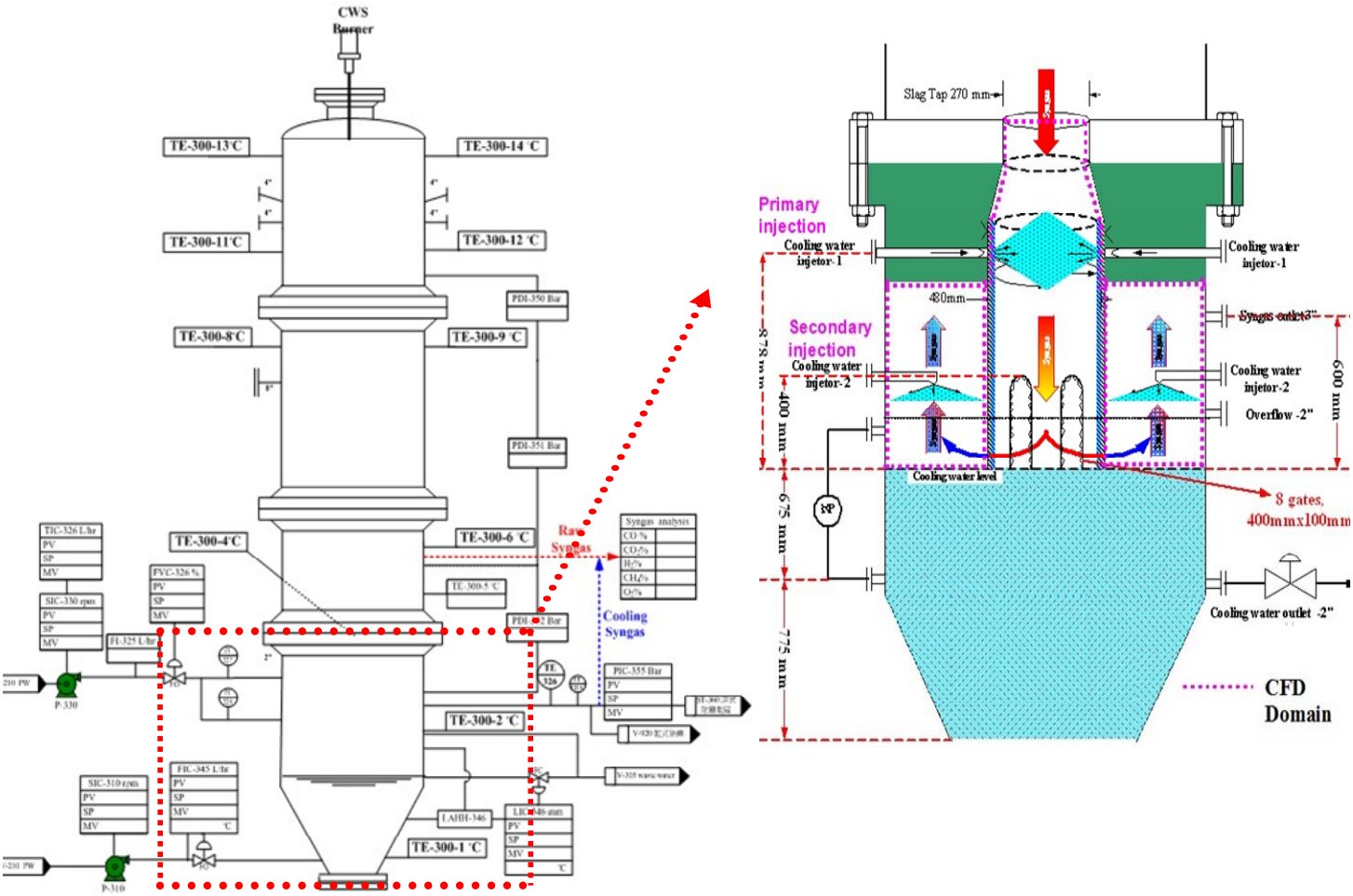

Fig. 1 (a) Schematic diagram of ITRI downdraft coal slurry-fed gasifier (b) gasifier's quench section showing locations of water injections: primary at the inlet and secondary in the outer annular.

2.0 COMPUTATIONAL MODEL

2.1 Governing Equations

The time-averaged, steady-state Navier-Stokes equations as well as the mass and energy conservation equations are solved. The governing equations for the conservations of mass, momentum, and energy are given as:

$$\frac{\partial}{\partial x_i}\left(\rho u_{ij}\right) = S_m \qquad (1)$$

$$\frac{\partial}{\partial x_i}\left(\rho u_i u_j\right) = \rho \bar{g}_j - \frac{\partial P}{\partial x_j} + \frac{\partial}{\partial x_i}\left(\tau_{ij} - \rho\overline{u_i' u_j'}\right) + F_j \qquad (2)$$

$$\frac{\partial}{\partial x_i}\left(\rho c_p u_i T\right) = \frac{\partial}{\partial x_i}\left(\lambda \frac{\partial T}{\partial x_i} - \rho c_p \overline{u_i' T'}\right) + \mu\Phi + S_h \qquad (3)$$

The symmetric stress tensor, τ_{ij}, is given by:

$$\tau_{ij} = \mu\left(\frac{\partial u_j}{\partial x_i} + \frac{\partial u_i}{\partial x_j} - \frac{2}{3}\delta_{ij}\frac{\partial u_k}{\partial x_k}\right). \qquad (4)$$

The equation for species transport is:

$$\frac{\partial}{\partial x_i}\left(\rho u_i C_j\right) = \frac{\partial}{\partial x_i}\left(\rho D_i \frac{\partial C_j}{\partial x_i} - \rho\overline{u_i' C_j'}\right) + S_j \qquad (5)$$

2.2 Turbulence Models

Various turbulence models have been considered in a similar study of coal slurry gasification by Silaen and Wang (2010). They found the RSM turbulence model provided the more reliable and consistent results, and the standard k-ε turbulence model is close to the RSM model but with a significant reduction of computational time. In this study, the standard k-ε turbulence model with enhanced wall function is therefore employed to save computational time.

Standard k-ε Model -- The standard k-ε model defines the Reynolds stresses as

$$-\rho\overline{u_i' u_j'} = \mu_t\left(\frac{\partial u_i}{\partial x_j} + \frac{\partial u_j}{\partial x_i}\right) - \frac{2}{3}\rho k\delta_{ij} \qquad (6)$$

where k is the turbulence kinetic energy, and μ_t is the turbulence viscosity given by

$$\mu_t = \rho C_\mu k^2 / \varepsilon \qquad (7)$$

where $C_\mu$is a constant and ε is the turbulence dissipation rate. The equations for the turbulence kinetic energy (k) and dissipation rate (ε) are

$$\frac{\partial}{\partial x_i}\left(\rho u_i k\right) = \frac{\partial}{\partial x_i}\left[\left(\mu + \frac{\mu_t}{\sigma_k}\right)\frac{\partial k}{\partial x_i}\right] + G_k - \rho\varepsilon \qquad (8)$$

$$\frac{\partial}{\partial x_i}\left(\rho u_i \varepsilon\right) = \frac{\partial}{\partial x_i}\left[\left(\mu + \frac{\mu_t}{\sigma_\varepsilon}\right)\frac{\partial \varepsilon}{\partial x_i}\right] + C_{1\varepsilon} G_k \frac{\varepsilon}{k} - C_{2\varepsilon} G_k \rho \frac{\varepsilon^2}{k} \qquad (9)$$

G_k is the generation of turbulence kinetic energy due to the mean velocity gradients. The turbulent heat flux and mass flux can be modeled with the turbulent heat conductivity (λ_t) and the turbulent diffusion coefficient (D_t), respectively.

$$\rho c_p \overline{u_i' T'} = -\lambda_t \frac{\partial T}{\partial x_i} = -c_p \frac{\mu_t}{Pr_t}\frac{\partial T}{\partial x_i}, \qquad (10)$$

$$\rho\overline{u'_i\, C'} = -\rho D_t \frac{\partial C}{\partial x_i} = -\frac{\mu_t}{Sc_t}\frac{\partial C}{\partial x_i}\,. \qquad (11)$$

The constants $C_{1\varepsilon}$, $C_{2\varepsilon}$, C_μ, σ_k, and $\sigma_\varepsilon$used are: $C_{1\varepsilon}$= 1.44, $C_{2\varepsilon}$ = 1.92, C_μ = 0.09, σ_k = 1.0 [Launder and Spalding, 1972]. The turbulent Prandtl number, Pr_t, is set to 0.85, and the turbulent Schmidt number, Sc_t, is set to 0.7.

Enhanced Wall Function – The above k-ε model is mainly valid for high Reynolds number, fully-turbulent flow. Special treatment is needed in the region close to the wall. The enhanced wall function is one of several methods that model the near-wall flow. In the enhanced wall treatment, the two-layer model is combined with the wall functions. The whole domain is separated into a viscosity-affected region and a fully turbulent region by defining a turbulent Reynolds number, Re_y,

$$Re_y = yk^{1/2}/\nu \qquad (12)$$

where k is the turbulence kinetic energy and y is the distance from the wall. The standard k-ε model is used in the fully turbulent region where $Re_y > 200$, and the one-equation model of Wolfstein [1969] is used in the viscosity-affected region with $Re_y < 200$. The turbulent viscosities calculated from these two regions are blended with a blending function (θ) to smoothen the transition.

$$\mu_{t,enhanced} = \theta\mu_t + (1-\theta)\mu_{t,l} \qquad (13)$$

where μ_t is the viscosity from the k-ε model of high Reynolds number, and $\mu_{t,l}$ is the viscosity from the near-wall one-equation model. The blending function is defined so it is equal to 0 at the wall and 1 in the fully turbulent region. The linear (laminar) and logarithmic (turbulent) laws of the wall are also blended to make the wall functions applicable throughout the entire near-wall region.

2.3 Discrete Phases (Liquid Droplets)

The droplets from the spray nozzles are considered as a discrete phase. The Langrangian method is adopted to track each particle in this study. Particles in the airflow can encounter inertia and hydrodynamic drags. Because of the forces experienced by a droplet in a flow field, the particles can be either accelerated or decelerated. The velocity change can be formulated as:

$$m_p d\mathbf{v_p}/dt = \mathbf{F_d} + \mathbf{F_g} + \mathbf{F_o} \qquad (14)$$

where F_d is the drag of the fluid on the droplet and F_g is the gravity. F_o represents the other body forces, typically include the "virtual mass" force, thermophoretic force, Brownian force, Saffman's lift force, etc**.** V_p is the particle velocity (vector). In this study, in addition to the main forces F_d and F_g, the Saffman's lift force is included in the calculation.

Theoretically, evaporation occurs at two stages: (a) when the droplet temperature is higher than the saturation temperature (based on local water vapor concentration), water evaporates from the particle's surface, and the evaporation is controlled by the water vapor partial pressure until 100% relative humidity is achieved and (b) when the boiling temperature (determined by the air-water mixture pressure) is reached, water continues to evaporate even after the relative humidity reaches 100%. After the moisture is evaporated due to either high temperature or low moisture partial pressure, the vapor diffuses into the main flow and is transported away. The rate of vaporization is governed by the concentration difference between surface and the main gas stream, and the corresponding mass change rate of the particle is given by:

$$\frac{dm_p}{dt} = \pi d^2 k_c (C_s - C_\infty) \qquad (15)$$

where k_c is the mass transfer coefficient and C_s is the concentration of the vapor at the particle's surface, which is evaluated by assuming that the flow over the surface is saturated. C_∞ is the vapor concentration of the bulk flow, obtained by solving the transport equations. The values of k_c can be calculated from empirical correlations by Ranz and Marshall [1955]:

$$Sh_d = \frac{k_c d}{D} = 2.0 + 0.6 Re_d^{0.5} Sc^{0.33} \qquad (16)$$

where Sh is the Sherwood number, Sc is the Schmidt number (defined as ν/D), D is the diffusion coefficient of vapor in the bulk flow. Re_d is the Reynolds number, defined as $u\nu/d$, u is the slip velocity, which is the velocity difference between the droplet and the flow.

When the droplet temperature reaches the boiling point, the following equation can be used to evaluate its evaporation rate [Kuo, 1985]:

$$\frac{dm_p}{dt} = \pi d^2 \left(\frac{\lambda}{d}\right)(2.0 + 0.46 Re_d^{0.5}) \ln\left(1 + c_p (T_\infty - T)/h_{fg}\right)/c_p \qquad (17)$$

where λ is the heat conductivity of the main gas-mixture stream, h_{fg} is the droplet latent heat, and c_p is the specific heat of the bulk flow.

The droplet temperature can also be changed due to heat transfer between droplets and the continuous phase. The droplet's temperature change depends on the convective and radiative heat transfer and latent heat (h_{fg}), as shown in the following equation:

$$m_p c_p \frac{dT}{dt} = \pi d^2 h(T_\infty - T) + \frac{dm_p}{dt} h_{fg} + f_h \frac{dm_p}{dt} H_{reac} - \nabla \cdot q_r \qquad (18)$$

where H_{reac} is the reaction heat of each chemical reaction. The term, $-\nabla \cdot q_r$, is the term of heat sources or sinks due to radiation which is calculated by:

$$-\nabla \cdot q_r = aG - 4a\sigma T^4 \qquad (19)$$

$$\text{where } q_r = -\frac{1}{3(a + \sigma_s) - C\sigma_s} \nabla G \qquad (20)$$

and q_r is the radiation heat flux, a is the absorption coefficient, σ_s is the scattering coefficient, G is the incident radiation, C is the linear-anisotropic phase function coefficient, and σ is the Stefan-Boltzmann constant. The P-1 method is used for calculating the radiative heat transfer. The P-1 radiation model is the simplest case of the more general P-N radiation model, but it only needs a fraction of computational time of the P-N method. Since the optical thickness (aL) of the current application is large, P-1 method is adopted, where "a" is the absorption coefficient and L is the length scale of the domain.

2.4 Reaction Models

The WGS reaction [Smoot and Smith, 1985] is given below:

<u>Homogenous gas phase</u>

$CO + H_2O\ (g) \leftrightarrow CO2 + H_2 \quad \Delta H°_R = -41.0$ MJ/kmol (Water-shift) (21)

For the gas phase reactions, both the eddy-dissipation and finite rates are calculated, and the slower rate will be used. The eddy-dissipation model takes into account the turbulent mixing of the gases. It assumes that the

chemical reaction is faster than the time scale of the turbulence eddies. Thus, the reaction rate is determined by the turbulent mixing of the species. The reaction is assumed to occur instantaneously when the reactants meet. The net rate of production or consumption of a species R_i is given by the smaller of the two expressions below.

$$R_i = \nu_i' M_i A \rho \frac{\varepsilon}{k} \min_R \left(\frac{Y_R}{\nu'_R M_{w,R}} \right) \quad (22)$$

$$R_i = \nu_i' M_i B \rho \frac{\varepsilon}{k} \left(\frac{\sum_P Y_P}{\sum_j^N \nu_j'' M_w} \right) \quad (23)$$

where ν_i' is the stoichiometric coefficient of the reactant i and ν_j'' is the stoichiometric coefficient of the product, j. The smaller of the two expressions (22) and (23) is used because it is the limiting value that determines the reaction rate.

The Finite rate model does not take into account the turbulent mixing of the species. The reaction rate is expressed through the Arrhenius form. The reaction rates in Arrhenius form for all of the gas phase reactions are given in Table 2. The reaction rate of the WGS reaction, adopted from Jones and Lindstedt [1998], is thought to be too fast in this study because the rate was experimentally obtained with the presence of a catalyst. The WGS rate under a non-catalytic condition has not been intensively investigated. Sato et al. (2004) experimentally investigated the rate constants for the WGS reaction kinetics under non-catalytic conditions in supercritical water and came up with the values of $A = 10^{5.58 \pm 1.38}$ and $E = 1.16 \times 10^5$ J/kmol for reaction at 653 K and at a pressure in the range of 25 to 30 MPa. Wade et al. (2008) conducted experiments on the WGS reaction process non-catalytically in the temperature range of 770 to 1050 K with an operating pressure of 24 MPa and arrived at the rate constants of $A = 2.512 \times 10^5$ and $E = 1.325 \times 10^5$ J/kmol. Silaen and Wang (2009) used Jones's rate and compared their CFD-simulated syngas results with that from the actual production of a commercial entrained-flow gasifier with coal slurry fed from the bottom. They found that the Jones's rate is too fast and they had to purposely slow down the reaction rate constant to $A = 2.75 \times 10^2$. Due to the unavailability of precise reaction rate constants, in the present study, all of these aforementioned rates are tested, and the results are compared against the experimental data individually. The exponential constant value (A) of each reaction rate is adjusted to match the experiment data.

2.5 Computational Domains

The computational domain of the quench section of the ITRI gasifier is shown in Fig. 2. The computational domain contains roughly 300,000 elements. FLUENT 12.0.16 is used as the CFD solver. The simulation uses the segregated solver, which employs an implicit pressure-correction scheme and decouples the momentum and energy equations. The SIMPLE algorithm is used to couple the pressure and velocity. The second-order upwind scheme is selected for spatial discretization of the convective terms and species. The computation is conducted for the continuous phase first. After obtaining an approximate, converged flow field of the syngas the droplet trajectories are calculated. At the same time, the drag, heat transfer, and mass transfer between the droplets and the syngas are calculated.

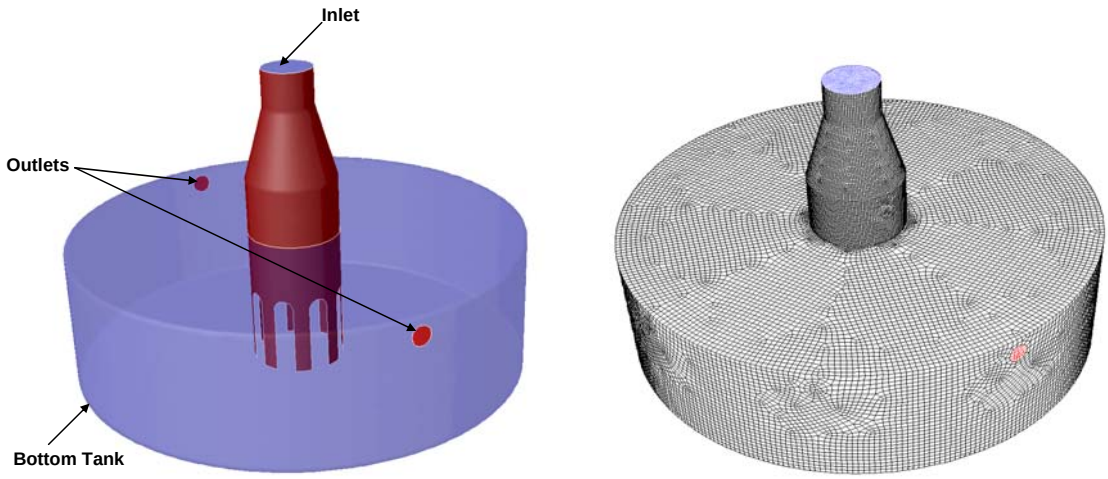

Fig. 2 Geometry, boundary conditions and meshed computational domain of the quench section of the ITRI Gasifier

2.6 Boundary Conditions and Inlet Conditions

Based on the experimental data, the mass flow rate of 0.04 kg/s and the composition of raw sysgas as shown in Table 3 are assigned as the inlet conditions at the top of the quench section. The entrance of the quench section connects to the bottom of the gasifer (Fig. 1). The temperature and pressure of the incoming flow are 954 K and 3 atm, respectively. The locations of the primary and secondary injectors are shown in Fig. 3.

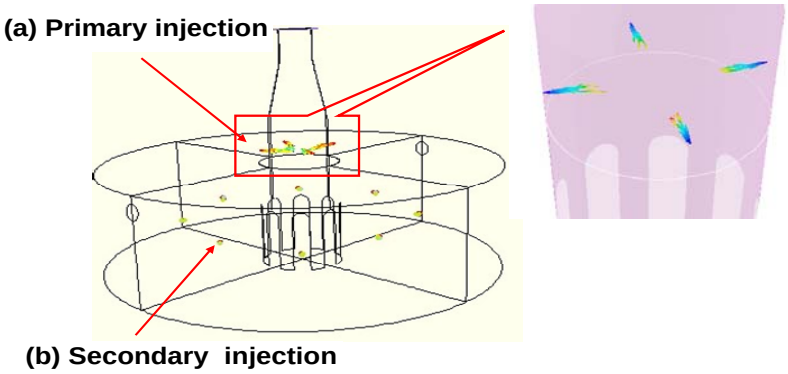

Fig. 3 Locations of water injections: (a) the primary injection consisting of two pairs of opposing jets and (b) the secondary injection consisting of eight injectors spraying downward against the up moving flow.

The walls are all set as adiabatic and with no slip (ie. velocity is zero), but the thermal boundary condition of the shell wall of the main chamber (i.e., the wall between the primary injection and secondary injection) is set as "coupled," which means the heat fluxes on both sides of the wall will be calculated and matched to obtain the net heat flux through the wall. The particles are assigned to reflect if they hit any wall. The operating pressure inside the gasifier is set at 3 atm. The outlet is set as a constant pressure condition at 1 atm. The syngas is considered to be a continuous flow, and the water from the spray is considered to be a discrete particle flow. The water droplets are all considered to be perfectly spherical with a uniform, arithmetic diameter of 10 μm. Although the actual size distribution of the atomized water droplets will be non-uniform, simulation using a uniform droplet size distribution provides a more convenient way to track the droplet evaporation process than a non-uniform droplet size distribution.

3.0 RESULTS AND DISCUSSION

In this paper, investigation of syngas as the inlet flow is carried out with a syngas mass flow rate of 0.04 kg/s, a temperature of 954 K, and a pressure of 3 atm. The syngas compositions and inlet conditions are taken from the ITRI experimental data.

3.1 Calibration of WGS Rates

As mentioned before, due to the uncertainty of the WGS reaction rate, three different reaction rates (Jones's rate under catalytic condition and Wade's and Sato's rates under non-catalytic conditions) are used with water spraying at the primary injection location with a flow rate of 0.0052 kg/s. The result in Table 2 shows that all the three reaction rates are too fast because most of CO has been converted to H_2 and CO_2, since the computed mole fractions of H_2 and CO_2 are higher than the experimental data while that of CO is lower. Also, because the reaction rates are too fast, the exit syngas almost reaches equilibrium and the results of all three rates are essentially identical. The CO conversion rate in Table 2 is defined as $(CO_{in} - CO_{out})/CO_{in}$, where CO_{in} is the mass flow rate of CO at inlet and CO_{out} is the mass flow rate of CO at outlet. Furthermore, the exit syngas temperature is approximately 173 K higher than the experimental data, indicating more heat is released from the WGS reaction. These discrepancies could be caused by the fact that this study employs the rates at different operating pressure and temperature ranges than those in the laboratory conditions under which the published rates themselves were derived.

To calibrate the reaction rates, the exponential constant, A, of each reaction rate is then progressively adjusted to lower values until the syngas composition matches the experimental data. An example of this process is shown in Table 3 by adjusting the A value of Wade's rate from 2.512×10^{5} to 2.512×10^{-5}. There is a large change of syngas composition from the case with $A = 2.512 \times 10^{5}$ to the case with $A = 2.512 \times 10^{-3}$, but no notable further change is seen after A is reduced to below 2.515×10^{-3}. The progressive change of syngas composition is shown in Fig. 4 which clearly shows that a faster rate produces more H_2 and CO_2, lower CO, and a higher exit temperature. Compared with the experimental data, the result of the CFD simulated case with $A = 2.512 \times 10^{-1}$ fairs best. The similar calibration process is applied to both Jones's and Sato's rates and all their results are listed in Table 4 for comparison. It appears that all of the original rates can be adjusted to a slower rate that can match the experimental gas composition data well. Without much preference between Sato's and Wade's rates, Wade's rate was chosen for the calibration with $A = 2.512 \times 10^{-1}$ and $E = 1.325 \times 10^{5}$ J/kmol under a non-catalytic condition. However, even though the experimental gas composition data have been matched well by the calibrated WGS reaction rate, the computed gas exit temperature is still about 170K higher than the experimental data. This temperature difference could be contributed by two possible reasons: (a) The heat loses through the real wall, which can't be perfectly insulated as assumed in the simulation model; (b) The additional gas cooling due to gas stream penetrating into the water bath is not included in the simulation model.

Note that the experimental data doesn't have the water vapor composition because a large part of the water vapor has condensed during the transportation of the sampled syngas to the gas analyzer. Therefore, the water vapor amount is not included in the comparison and the syngas composition of the simulated CFD results are renormalized by taking off the water vapor component.

Table 2 CFD simulated syngas composition using three original published WGS reaction rates (Note, experimental water vapor data is not available for comparison.)

Primary injection	Experimental data	$A=2.75\times10^{10}$ $E=8.38\times10^{7}$ J/kmol Jones et al. (1998)	$A=10^{5.58\pm1.38}$ $E=1.16\times10^{5}$ J/kmol Sato et al. (2004)	$A=2.512\times10^{5}$ $E=1.325\times10^{5}$ J/kmol Wade et al. (2008)
Syngas composition	Exit Mole Fraction			
H_2	0.36	0.50	0.49	0.49
CO_2	0.29	0.46	0.45	0.45
CO	0.34	0.03	0.05	0.05
CH_4	0.01	0.01	0.01	0.01
CO conversion (%)		88	80	80
Temperature (K)	673	948	944	946

Table 3 Effect of WGS rate constants on quenched syngas composition by changing A value of Wade's rate (Note, experimental water vapor data is not available for comparison)

Primary injection	Experimental data	$A=2.512\times10^{5}$ $E=1.325\times10^{5}$ J/kmol	$A=2.512\times10^{0}$ $E=1.325\times10^{5}$ J/kmol	$A=2.512\times10^{-1}$ $E=1.325\times10^{5}$ J/kmol	$A=2.512\times10^{-3}$ $E=1.325\times10^{5}$ J/kmol	$A=2.512\times10^{-5}$ $E=1.325\times10^{5}$ J/kmol
Syngas composition	Exit mole fraction					
H_2	0.36	0.49	0.46	0.37	0.32	0.32
CO_2	0.29	0.45	0.41	0.30	0.25	0.25
CO	0.34	0.05	0.12	0.32	0.42	0.42
CH_4	0.01	0.01	0.01	0.01	0.02	0.02
CO conversion (%)		80	62	16	2	2
Temperature (K)	673	946	864	875	857	848

Table 4 CFD simulated syngas composition using three calibrated WGS reaction rates (Note, experimental water vapor data is not available for comparison)

Primary injection	Experimental data	$A=2.75\times10^{3}$ $E=8.38\times10^{7}$ J/kmol	$A=10^{-1}$ $E=1.16\times10^{5}$ J/kmol	$A=2.512\times10^{-1}$ $E=1.325\times10^{5}$ J/kmol
Syngas Composition	Exit mole fraction			
H_2	0.36	0.36	0.34	0.37
CO_2	0.29	0.28	0.29	0.30
CO	0.34	0.38	0.36	0.32
CH_4	0.01	0.01	0.01	0.01
CO conversion (%)		8	10	16
Temperature (K)	673	842	864	875

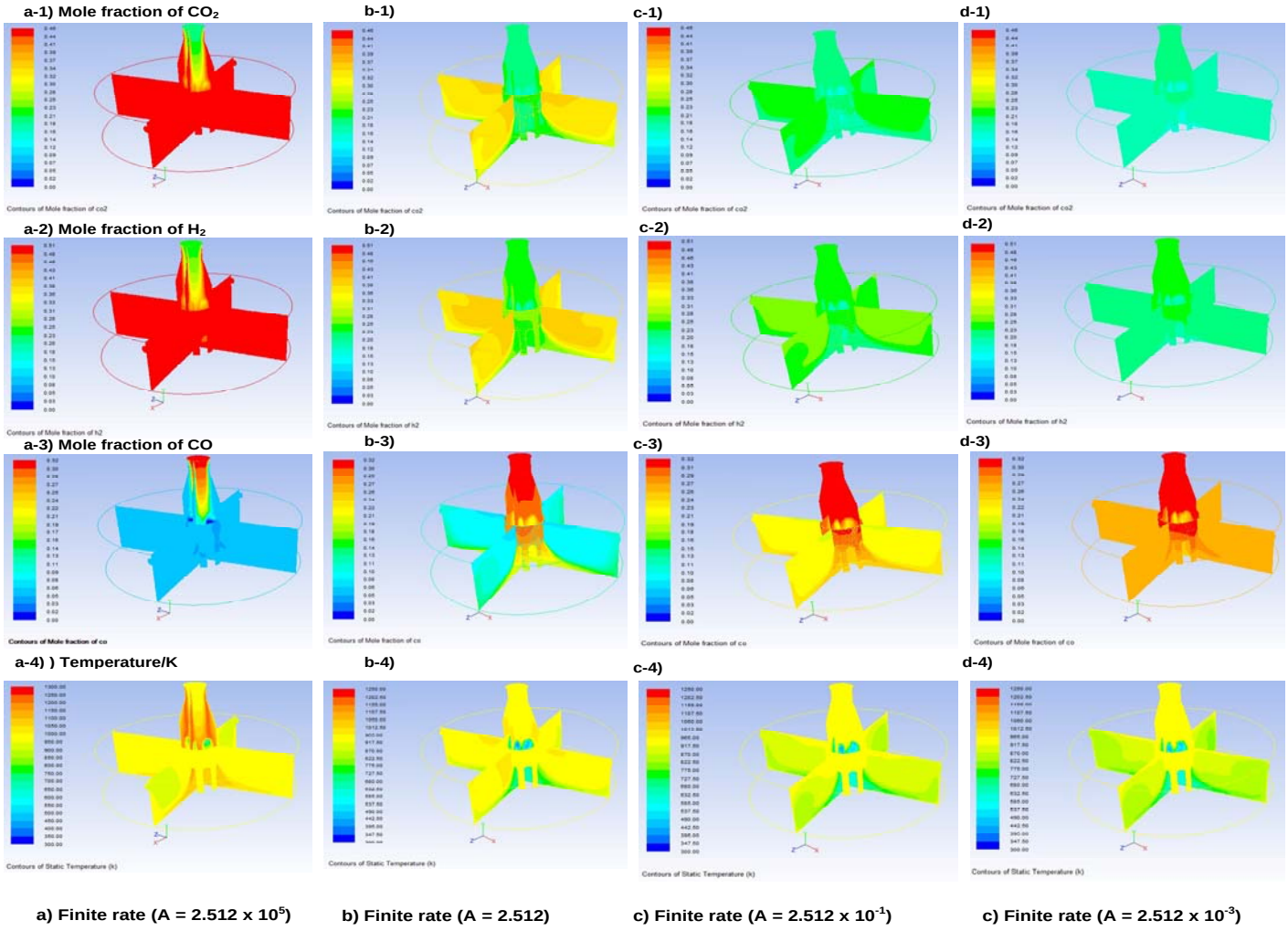

Fig. 4 Variation of Temperature and syngas composition by changing the A value of Wade's rate with the primary water injection. Faster rates produce more H_2 and CO_2, lower CO, and higher temperature.

3.2 Effect of the Primary vs. the Secondary Injection

After calibration of the WGS rate is accomplished, the CFD model becomes a useful tool to help investigate parametric study interests. The first interest falls in examining the WGS performance of injecting water at the primary and secondary location, respectively. In these simulations, two cases are conducted: one with the total water injection of 0.0052 kg/s at the primary injection location alone and the second case with the same amount of water injection at the secondary injection alone. The simulation calculations are performed until the mass fractions of the various species are stabilized. The velocity contour and velocity vector plots of syngas at two different mid-planes placed perpendicular to each other are shown in Fig. 5.

It is clear from Fig. 5a that the syngas flow is been obstructed by the primary water injection in the main chamber when the primary injection is used. Figure 5b shows the change in flow field when the water spraying is switched from the primary to the secondary injection location. Selected syngas flow pathlines for the primary and secondary injection cases are shown in Fig. 6. From the flow pattern shown in both Figs. 5 and 6, the flow field is seen to be highly 3-D, consisting of complex vortices.

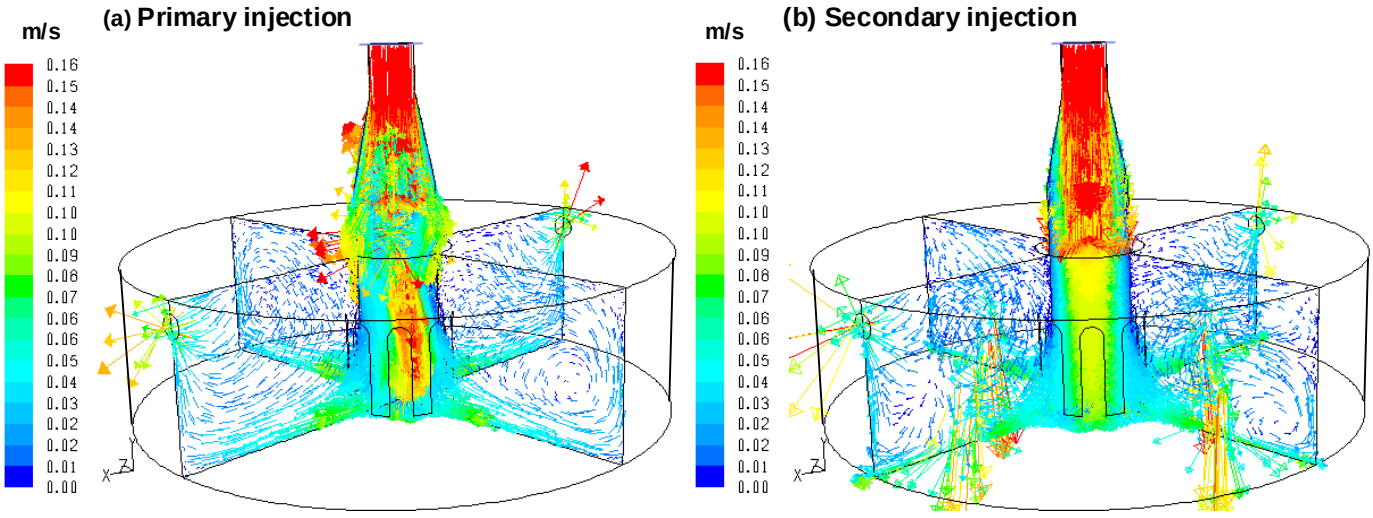

Fig. 5 Velocity vector fields on two selected planes for primary and secondary injection cases, respectively

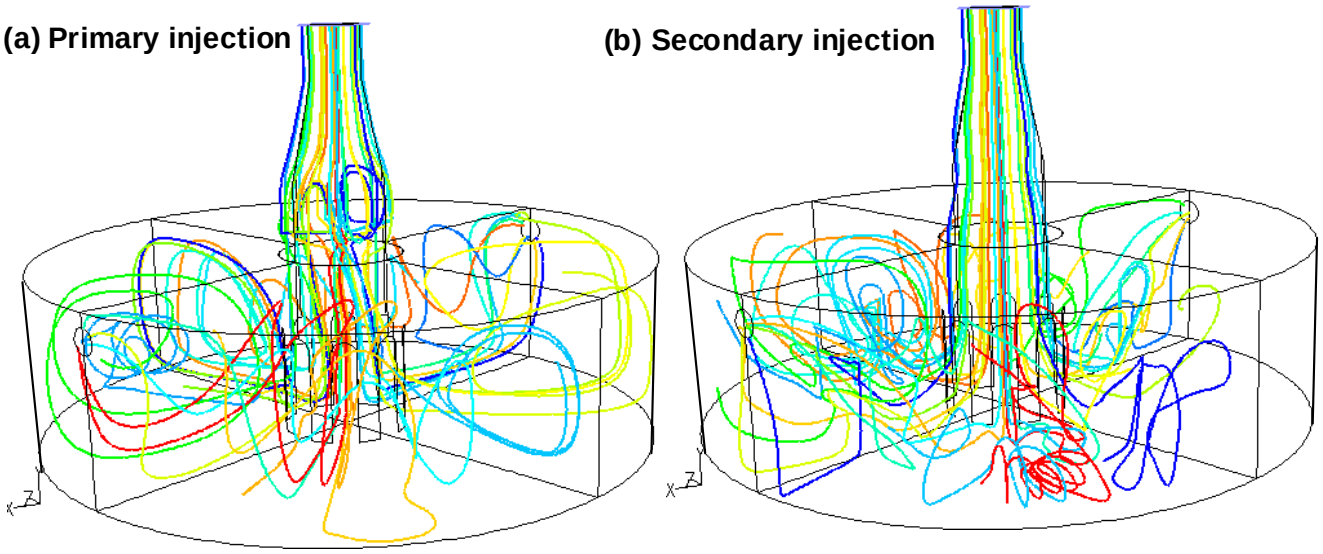

Fig. 6 Syngas pathline for primary and secondary injection cases.

The CO_2, H_2, and temperature distributions for the primary water injection and secondary water injection cases are shown in Fig. 7. The syngas composition and temperature at outlet for both cases are listed in Table 5. The CO conversion (%) is approximately 16% in both cases. The primary injector seems slightly better in producing a higher H_2 concentration and high heating value (HHV) than the secondary injection. This slightly better WGS reaction is also reflected by the higher exit temperature for the primary injection case (875 K versus 844K) due to the exothermic behavior of the forward WGS reaction. Figure 7 shows the side-by-side comparison of temperature and multiple species distributions between these two cases.

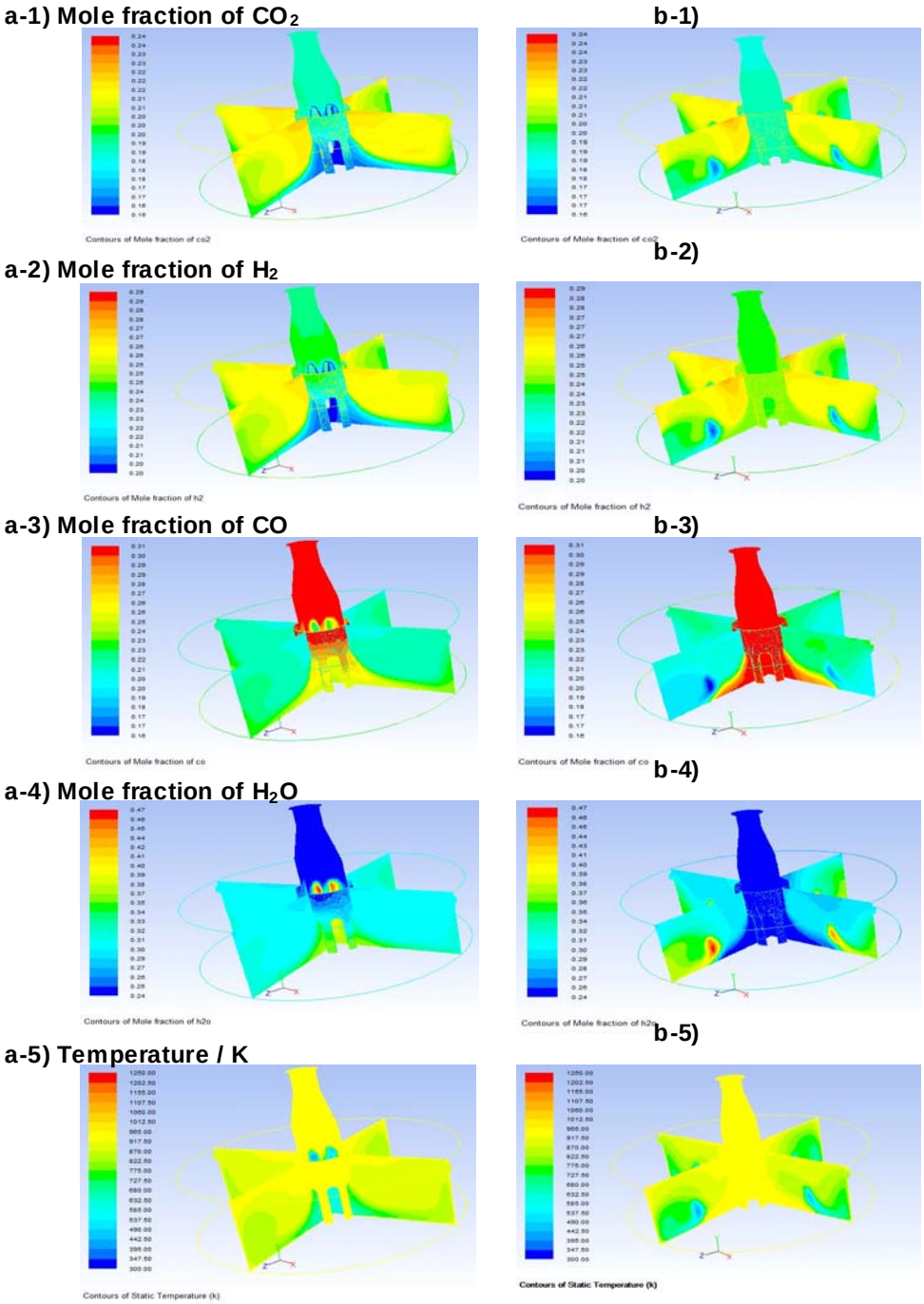

Fig. 7 Distributions of temperature and various species on two selected planes for primary and secondary injection cases using reaction rate A= 0.2512 E = 1.325 x 10^5 J/kmol

Table 5 Effect of water injection location on syngas composition using reaction rate A= 0.2512 E = 1.325 x 10^5 J/kmol

Mole fraction	Inlet	Primary injection outlet	Secondary injection outlet
H_2	0.24	0.26	0.25
CO_2	0.19	0.21	0.21
CO	0.31	0.22	0.22
CH_4	0.01	0.01	0.01
H_2O	0.25	0.30	0.31
Temp (K)	954	875	844
HHV(Base on 298K)		194 MJ/kmol (9.03MJ/kg)	188 MJ/kmol (8.69MJ/kg)

3.3 Effect of Water Level Gap in the Bottom Tank

As mentioned in the Introduction, the water bath level can be adjusted higher or lower to allow the raw syngas to penetrate into the water bath at different depths to further reduce snygas temperature, augment the WGS process, and remove soot or dust. Simulation of a gas stream penetrating into a liquid bath requires the employment of multiphase modeling using the Eulerian-Eulerian method. Coupling a Langrangian-Eulerian method, which tracks each individual liquid particle, with an Eulerian-Eulerian method which uses the void fraction to represent the gas and liquid composition separately, is a great challenge and beyond the scope of this paper. Therefore, the simulation is simplified by treating the gas-liquid interface as a wall which can't be penetrated. Although the phenomenon of gas penetrating into the liquid bath is not simulated, the simplified simulation can capture the effect of the water level height by calculating the changing flow velocity as the opening gaps are widened or narrowed due to changing water bath levels. As the gas flow accelerates through narrower openings, it is hypothesized that the WGS reaction could be increased and the heat transfer between the syngas and the water bath could increase, too. If this is true, controlling the water level would become an easy and low-cost method to fine-tune the exit syngas composition without using additional water. This is the motivation for studying the effect of the water level and for hoping to find an optimum level gap via CFD simulation.

The simulation results discussed in the previous sections consider the water level of 873mm from the primary injection location (water level gap). In addition to the baseline case of 873 mm, two additional cases with two different water level gaps including 700 mm and 1,050 mm are considered. The products and temperature distributions for these three cases are shown in Fig. 8 and Table 6. The result is listed in Table 6 and it shows that when the gap decreases from 1050 to 700 mm, the H_2 production decreases instead increases as previously hypothesized. The CO conversion rate decreases 7 percentage points (or 35%) from 20% to 13%, and the syngas outlet temperature decreases from 891 K to 871 K, correctly reflecting the decreased heat released during the WGS reaction. The trend of changing water level gaps on the WGS process is plotted in Fig. 9. The CO conversion rate varies almost linearly with the gap width. It then becomes interesting to find out why the previous hypothesis is not correct. After a few explorations, it is discovered that as the gases move faster through the narrower gaps, the average residence time decreases 11%: correspondingly from 0.396s to 0.355s, which results in less time for the WGS reaction to take place. Although the result is opposite to the previous hypothesis, it indicates that the water bath level could be used to control H_2 production within 1 percentage point (or 4%) without resorting to using a water spray. However, it needs to be emphasized that this result needs to be verified by experiments because the complex phenomenon of a gas stream penetrating into the water bath is not modeled in this study.

Table 6 Effect of water level gap on WGS using reaction rate A= 0.2512 E = 1.325 x 105 J/kmol

Mole fraction	Inlet	Gap (700mm)	Gap (873mm)	Gap (1050mm)
H_2	0.24	0.25	0.26	0.26
CO_2	0.19	0.20	0.21	0.22
CO	0.31	0.23	0.22	0.21
CH_4	0.01	0.01	0.01	0.01
H_2O	0.25	0.31	0.31	0.30
CO conversion (%)		13	16	20
Temperature (K)	954	871	875	891
Average residence time (s)		0.355	0.373	0.396
HHV in kJ/kmol (Base on 298K)		191,045	193,524	190,424

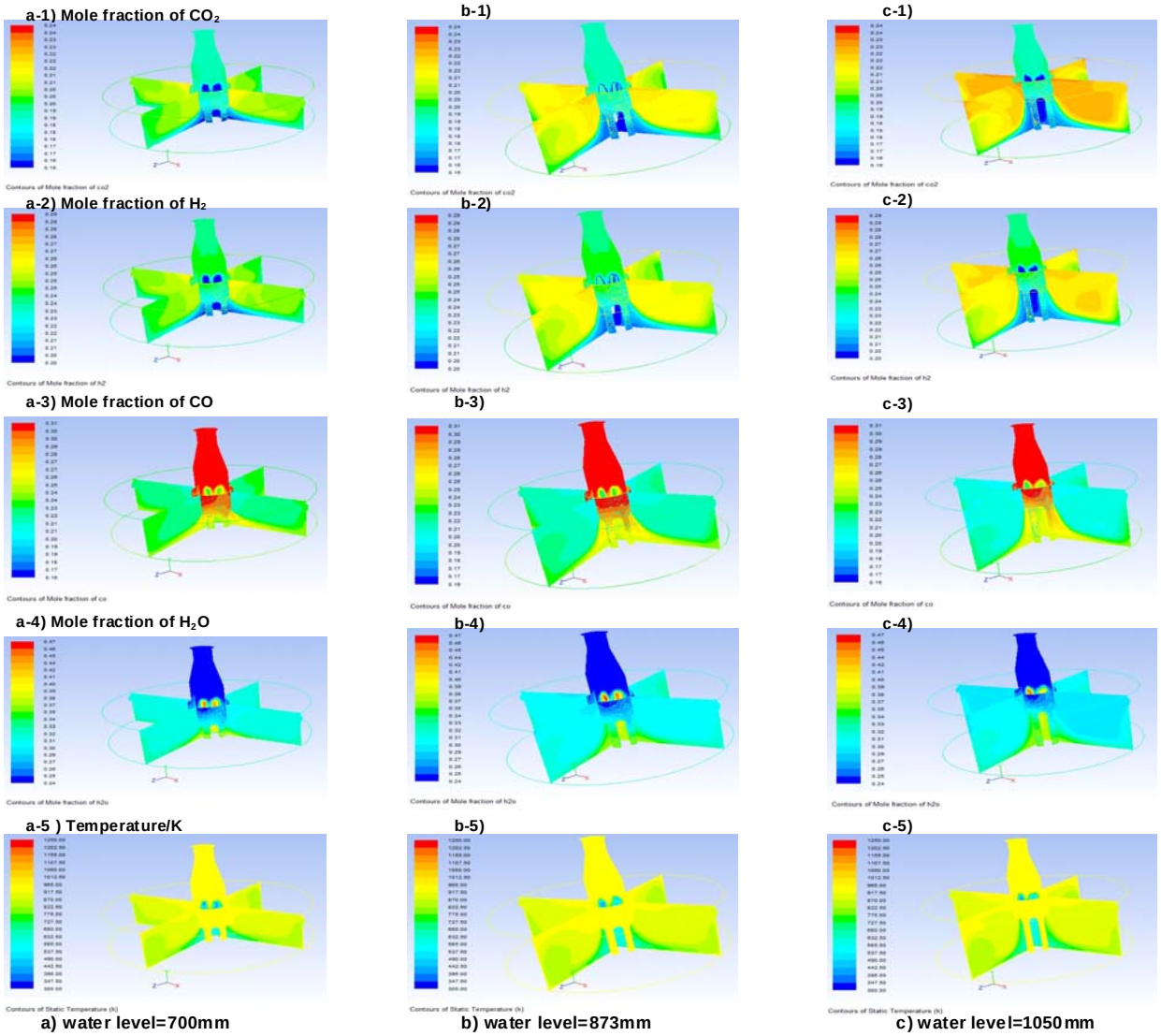

Fig. 8 Distribution of various species for three different water bath level gaps

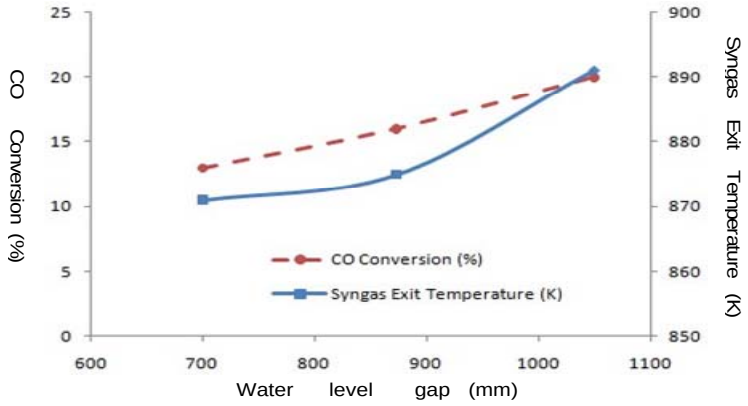

Fig. 9 Effect of water level gap on WGS and syngas temperature using reaction rate A= 0.2512 E = 1.325 x 10^5 J/kmol

4.0 CONCLUSIONS

A CFD model has been developed to investigate the water quench section design of an oxygen-blown, slurry-fed, entrained flow coal gasifier. In the water quench section, the most important reaction is the WGS reaction. Three different published reaction rates (Jones's rate under a catalytic condition and Wade's and Sato's rates under a non-catalytic condition) are found to be too fast when the CFD results are compared with the experimental data, possibly due to employing the rates at different operating temperature and pressure conditions in the gasifer than those in the laboratory in which the rates themselves were derived. A calibration process was then conducted to progressively reduce the exponential constant, A, in the reaction rate equation to a lower value until the CFD result matched the experimental data. It was found that all three rates could be calibrated to match the experimental data. Finally, a modified version of Wade's rate (A= 0.2512 E = 1.325 x 10^5 J/kmol) was chosen for all of the parametric studies in this paper.

The effect of injection locations (primary vs. secondary) on the WGS reaction is marginal. Both locations result in a 16% CO conversion rate. Spraying water in the primary location only provides a marginal advantage with an increase of 4% in H_2 production, 3% in HHV value, and 30K in temperature**.**

Using the water bath level to fine-tune the WGS is workable. When the water level gap decreases from 1050mm to 700 mm, the CO conversion rate decreases by 7 percentage points (or 35%) from 20% to 13%, and the syngas outlet temperature decreases by 20K (from 891 K to 871 K.) Beyond the gap of 1050mm, the effect of the water bath level is not noticeable.

5.0 ACKNOWLEDGMENT

This study was partially supported by the Louisiana Governor's Energy Initiative via the Clean Power and Energy Research Consortium (CPERC) and was administered by the Louisiana Board of Regents. The ITRI gasifier was funded by the Taiwan Bureau of Energy.

6.0 REFERENCES

Duan, R., Koshizuka, S. and Oka, Y., 2003 "Droplet Breakup Under Impulsive Acceleration Using Moving Particle semi-Implicit Method" 11 th International Conference on Nuclear Engineering, Tokyo, Japan, April 20-23, 2003, Paper No: ICONE11-36029.

FLUENT 6.3 User's Guide, September 2006.

Jones, W.P.and Lindstedt, R.P. "Global Reaction Schemes for Hydrocarbon Combustion, " Combustion and Flame, 73, 233, 1998.

Kuo, K. Y., 1986, *Principles of combustion*, John Wiley and Sons, New York.

Lauder, B.E., and Spalding, D.B., Lectures in Mathematical Modeling of Turbulence, Academic Press, London, England, 1972.

Martula, D.S., Hasegawa, T., Lloyd, D.R. and Bionnecaze, R. T., 2000, "Coalescence-Induced Coalescence of Inviscid Droplets in a Viscous Fluid" Journal of Colloid and Interface Science 232, 241–253.

O'Rourke, P. J. and Amsden, A. A., 1987, "The Tab Method for Numerical Calculation of Spray Droplet Breakup" SAE Technical Paper 872089, 1987.

O'Rourke, P. J., 1981, "Collective Drop Effects on Vaporizing Liquid Sprays" PhD dissertation, Princeton University, , New Jersey, 1981.23.

Pan, Y. and Suga, K., 2005, "Numerical Simulation of Binary Liquid Droplet Collision" Physics of Fluids 17, 082105.

Qiang, L. I., Ti-min C. A. I, Guo-qiang, H. E. and Chunbo, H. U., 2006, "Droplet Collision and Coalescence Model" Applied Math and Mechanics, 27(1):67–73.

Ranz, W. E. and Marshall Jr. W. R., 1952, "Evaporation From Drops Part I", *Chem. Eng. Prog*, Vol. 48, pp. 141-146.

Sato, T., Kurosawa S., Smith, R. L., Adschiri, T., Arai, K., 2004, "Water Gas Shift Reaction Kinetics under Noncatalytic Conditions in Supercritical Water" J. of Supercritical Fluids, 29, 113-119.

Silaen, A. and Wang, T., Simulation of Coal Gasification Process Inside a Two-Stage Gasifier, Paper 20-1, Proceedings of the 22nd Pittsburgh Coal Conference, Pittsburgh, Pennsylvania, September 19-22, 2005.

Silaen, A. and Wang,T., "Effects of Fuel Injection Angles on Performance of A Two-Stage Coal Gasifier," Paper 20-4, Proceedings of the 23rd Pittsburgh Coal Conference, Pittsburgh, Pennsylvania, September 25-28, 2006.

Silaen, A. and Wang,T., " Effect of Turbulence Models on Gasification Simulation " Paper 19-3, presented at the 25th International Pittsburgh Coal-Gen Conference, Pittsburgh, Pennsylvania, Sept. 29-Oct. 2, 2008

Silaen, A. and Wang, T., "Effect of Turbulence and Devolatilization Models on Gasification Simulation," International Journal of Heat and Mass Transfer, vol. 53, pp.2074-2091, 2010.

Smoot, D.L., and Smith, P.J., Coal Combustion and Gasification, Plenum Press, 1985.

Stegeman, Y.W., Chesters, A.K., vd Vosse, F.N. and Meijer, H.E.H., 1999, "Breakup of (non-) Newtonian droplets in a time-dependent elongational flow" Proceedings PPS-15's-Hertogenbosch, 1999.

Wang, T. and Silaen, A., 2009, “Numerical Investigation of Top Fuel Injection Design in a Coal Gasifier,” Paper 26-2, Proceedings of the 26th International Pittsburgh Coal Conference, Pittsburgh, USA, September 20-23.

Wang,T., Silaen, A., Hsu, H. W., and Lo, M. C., " Partial Load Simulation and Experiments of a Small Coal Gaifier," Paper 20-3, presented at the 23rd International Pittsburgh Coal-Gen Conference, Pittsburgh, Pennsylvania, Sept. 25-28, 2006.

Wade J P., Evar W, T., Bryan, L, H., Sunggyu, L.,2008, “Kinetics of Noncatalytic Water Gas Shift reaction in a supercritical Water Medium”, American Institute of Chemical Engineers AIChE Proceedings of the 2008 AIChE Spring National Meeting, April 2008: paper #139e.

Wolfstein, M., 1969, “The Velocity and Temperature Distribution of One-Dimensional Flow with Turbulence Augmentation and Pressure Gradient,” Int. J. Heat Mass Transfer, 12, pp. 301-318.